LANGMUIR

UQ LIBRARY

Subscriber access provided by UQ Library

Interfaces: Adsorption, Reactions, Films, Forces, Measurement Techniques, Charge Transfer, Electrochemistry, Electrocatalysis, Energy Production and Storage

Influence of Interfacial Gas Enrichment on Controlled Coalescence of Oil Droplets in Water in Microfluidics

Jianlong Wang, Adrian J.T. Teo, Say Hwa Tan, Geoffrey M. Evans, Nam-Trung Nguyen, and Anh V. Nguyen

Langmuir, **Just Accepted Manuscript** • DOI: 10.1021/acs.langmuir.8b03486 • Publication Date (Web): 12 Feb 2019

Influence of Interfacial Gas Enrichment on Controlled Coalescence of Oil Droplets in Water in Microfluidics

Jianlong Wang,[a] Adrian J. T. Teo,[b] Say H. Tan,[b] Geoffrey M. Evans,[c] Nam-Trung Nguyen,[b] Anh V. Nguyen*[a]

[a]School of Chemical Engineering, The University of Queensland, Brisbane, Queensland 4072, Australia
[b]Queensland Micro- and Nanotechnology Centre, Griffith University, Brisbane, Queensland 4111, Australia
[c]School of Engineering, The University of Newcastle, Callaghan, New South Wales 2308, Australia

*Corresponding authors
E-mail address: anh.nguyen@eng.uq.edu.au (A. V. Nguyen)

Abstract

Interfacial gas enrichment (IGE) of dissolved gases in water is shown to govern the strong attraction between solid hydrophobic surfaces of an atomic force microscopy (AFM) colloidal probe and a solid substrate. However, the role of IGE in controlling the attraction between fluid-fluid interfaces of foam films and emulsion films is difficult to establish by AFM techniques due to the extremely fast coalescence. Here, we applied droplet-based microfluidics to capture the fast coalescence event under the creeping flow condition and quantify the effect of IGE on the drainage and stability of water films between coalescing oil droplets. The amount of dissolved gases is controlled by partially degassing the oil phase. When the amount of dissolved gases (oxygen) in oil decreases (from 7.89 mg/L to 4.59 mg/L), the average drainage time of coalescence significantly increases (from 19 ms to 50 ms). Our theoretical quantification of the coalescence by incorporating IGE into the multilayer van der Waals attraction theory confirms the acceleration of film drainage dynamics by the van der Waals attractive force generated by IGE. The thickness of the IGE layer decreases from 5.5 nm to 4.9 nm when the amount of dissolved gas decreases from 7.89 mg/L to 4.59 mg/L. All these results establish the universal role of dissolved gases in governing the strong attraction between particulate hydrophobic interfaces.

***Keywords**:* water film, dissolved gases, IGE, van der Waals force

Nomenclature

A	Hamaker function (J)	y	Dimensionless thickness (-)
c	Speed of light (m/s)	y_0	Dimensionless thickness at time zero (-)
C	Number concentration of z:z salt ions (-)	z	Valency of ions (-)
Ca	Capillary number (-)		

d	IGE thickness (m)	ε_m	Dielectric function of water (-)
e	Charge of an electron (C)	ε_j	Dielectric function of material j (-)
h	Thickness (m)	κ	Debye constant (m^{-1})
h_i	Initial film thickness to offset zero drainage time (m)	Π	Disjoining pressure due to surface forces (Pa)
h_0	Thickness at time zero (m)	Π_{vdW}	van der Waals disjoining pressure (Pa)
i	Imaginary number (-)	Π_{EDL}	Electrical double layer disjoining pressure (Pa)
I	Ionic strength (mol/L)	μ	Water dynamic viscosity (Pa s)
k_B	Boltzmann constant (m^2 kg s^{-2} K^{-1})	$\overline{\mu}$	Mean of Gaussian fit (s)
n	Dimensionless index used in Eq. (2) (-)	ρ	Dimensionless radial coordinate (-)
p	Dimensionless excess pressure in the film relative to the bulk (-)	σ	Equilibrium interfacial tension (N m^{-1})
P	Excess pressure in the film relative to the bulk (Pa)	$\overline{\sigma}$	Standard deviation of Gaussian fit (s)
q	Parameter defined by Eq. (6) (-)	τ	Dimensionless time (-)
r	Radial coordinate in Eqs. (8) and (9) (m)	τ_0	Dimensionless time constant (-)
R	Effective radius of droplet (m)	ω	Matsubara frequency (Hz)
s_j	Retardation coefficient defined by Eq. (5) (-)	Δ_{jk}	Diamagnetic reflection coefficient between materials j and k (-)
t	Time (s)	$\overline{\Delta}_{jk}$	Dielectric reflection coefficient between materials j and k (-)
t_0	Time constant (s)	Φ	Dimensionless number in Eq. (16)
T	Absolut temperature (K)	ψ_s	Film surface potential (V)
T_1	Moment of droplet contact (s)	$\wp$	Dimensionless disjoining pressure (Pa)
T_2	Moment of water film rupture (s)	h	Planck constant divided by 2π (m^2 kg s^{-1})
V	Velocity constant (m/s)	$\sqrt{\Im}$	Diamagnetic reflection coefficients of a photon passing through the water film and IGEs from one droplet to another (-)
x	Integration dummy in Eq. (2) (-)	$\sqrt{\overline{\Im}}$	Dielectric reflection coefficients of a photon passing through the water film and IGEs from one droplet to another (-)
x_n	Lower limit of the integral in Eq. (2) (-)		

INTRODUCTION

Hydrophobic interactions are ubiquitous in water-based systems in our daily activities, from salad dressing and cleaning action of shampoos and detergents to phenomena related to

industrial practices, such as attachment of hydrophobic particles to air bubbles in froth flotation and protein folding for biotechnology. However, the origin of hydrophobic interactions has remained controversial for more than 30 years. The complexity of the hydrophobic interaction originates from a number of concomitant mechanisms. Despite contentious experimental validation, several mechanisms have been proposed. The mechanisms reported in the literature include the entropic origin, resulting from the rearrangement of water structure near the hydrophobic surfaces,[1-4] the nanobubble bridging capillary forces,[5-7] the cavitation (separation-induced phase transition),[8-17] the hydrodynamic origin,[18] and electrostatic origin.[19-20] A brief review of direct force measurements between hydrophobic surfaces in aqueous solutions has also been reported.[4] This review concluded that only the short-range hydrophobic attraction (<100 Å) represents the true hydrophobic interaction.

Dissolved gases have shown a significant effect on the strong attraction between hydrophobic surfaces. Except for the extensively documented effect of bridging nanobubbles and cavitation on the long-range attractive forces, a recent study found the interfacial gas enrichment (IGE) of dissolved gases significantly contributes to the short-range attractive forces between solid hydrophobic surfaces of an atomic force microscopy (AFM) probe and a hydrophobic solid substrate.[21] The existence of IGE is also examined by molecular dynamics simulation[22] and experimentally confirmed by the reduced water density at hydrophobic surfaces in the presence of dissolved gases observed via direct non-invasive neutron reflectivity measurements.[23] In addition, the intrinsic structure of water next to the oil phase has been proved to be similar to the bare water-vapor interface using molecular dynamics simulations of realistic models of alkanes and water.[24] However, the role of IGE in controlling the attraction between fluid-fluid interfaces of foam films and emulsion films is difficult to establish by AFM techniques due to the extremely fast coalescence.

Experimental techniques with high-precision measurements at different length scales can provide temporal and spatial information on interactions between fluid-fluid interfaces and are crucial to quantitative analysis using theoretical models. Experimental studies on interactions between fluid-fluid interfaces include the measurements of (i) film thickness variations with time by thin liquid film micro-interferometry[25-26], (ii) time-dependent forces

by AFM[21], and (iii) coalescence time by bubble pair method.[27] The measurements of (i) provide the variations of the local thickness (< 0.5 μm) with time and with position but are limited by many uncertainties due to the contamination, evaporation, and thermal or mechanical fluctuations from the environment. The measurements of (ii) provide valuable data of surface forces for comparison with theory but the procedures are tedious. The measurements of (iii) provide the lifetime of a liquid film. Recently, microfluidic method equipped with high-speed camera imaging shows its advantages over other techniques because of the faster and more efficient measurements of coalescence process.[28] The small scale and confinement of microfluidics channels minimizes evaporation, thermal or mechanical fluctuations from environment and possible contamination. The well-controlled generation and transport of micro-droplets provide an ideal (direct) observation of the well-controlled coalescence process under the creeping flow condition matching excellently the modelling approximation.

In this paper, we exploit microfluidics equipped with high speed camera imaging to measure the drainage time of film rupture (coalescence time) with hundreds of coalescence events for systems with two different amounts of dissolved gases. The confinement in a microchannel ensures a well-controlled transport of micro-droplets and film drainage process for quantitative analysis via theoretical models. We elucidate the effect of IGE on coalescence dynamics between two oil droplets by applying the advanced theory on the van der Waals interaction in the presence of IGE.

MATERIALS AND METHODS

Deionized (DI) water was obtained from a centralized distillation tap where the conductivity was 1.6×10^{-4} S/m at 20°C measured using a conductivity meter (HI5521-02, Hanna Instruments). The oil used was squalene (98%, S3626 Sigma-Aldrich, USA), which is a highly unsaturated hydrocarbon (C30H50) and contains large amounts of dissolved gases (concentration of air soluble in oil is about 10 times higher than that in water).[26] Squalene was used as purchased. The dynamic viscosity and equilibrium interfacial tension of the unpurified squalene against water at 20 °C were μ = 0.012 Pa.s and σ = 0.0153 N/m,

respectively.[29] The amount of dissolved gases was manipulated by gassing or degassing the oil. The oil was exposed to clean air over night for gassing and dissolved oxygen was measured to indicate the dissolved gas content. The oil was saturated with air by exposure to open-air for 12 hours in a small glass dish. Under these conditions it was very unlikely that any squalene oxidation occurred given that oxidation of squalene only starts after 8 days at 62 °C under continuous air flow.[30] The oil was placed into a vacuum chamber for two hours to degas. Vacuum was supplied using a centralized vacuum system. A dissolved oxygen probe (Pro20 Dissolved Oxygen Instrument, YSI, USA) with a polarography sensor was used to measure the dissolved oxygen concentrations in gassed and degassed oils. As the contact between oil and air was inevitable during the measurements, only partial removal of dissolved gases was achieved. The dissolved oxygen concentrations for the gassed and partially degassed oils were 7.89 ± 0.01 mg/L and 4.59 ± 0.01 mg/L, respectively. To minimize the fluctuation of dissolved gas content, the oil sample was insulated by the gas-tight glass syringe and microfluidic channels against the open air during the measurements.

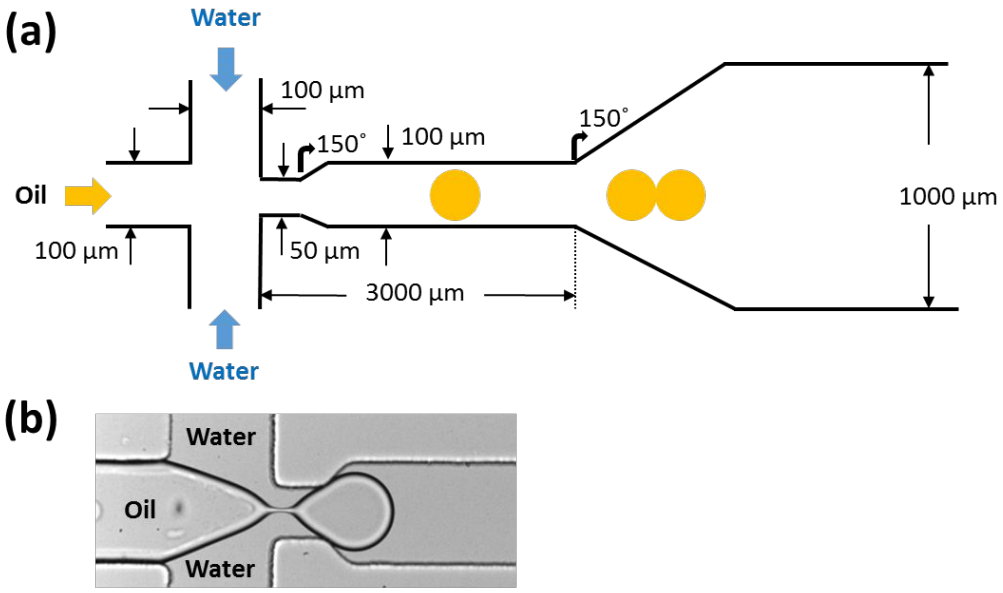

Figure 1. A microfluidic device for examining the effect of IGE on droplet coalescence: (a) Schematic diagram of a flow-focusing microfluidic device. (b) Micrograph of oil (gassed) droplet generation with a total water flow rate 200 µL/h and oil flow rate 10 µL/h.

A soft lithography technique was used to fabricate the microfluidic device in poly dimethylsiloxane (PDMS).[31] PDMS devices were irreversibly bonded to a glass slide using the air plasma. The widths of main channels and orifice were 100 and 50 μm, respectively (Figure 1). The height of the microchannel was about 30 μm. Flow rates of water and oil were adjusted to 200 and 10 μL/h, respectively. Droplet generation was performed with optimal wetting conditions. Sequential layer-by-layer polyelectrolyte deposition, by poly(allylamine hydrochloride), (98%, Sigma-Aldrich, USA) and poly(sodium 4-styrenesulfonate), (98%, Sigma-Aldrich, USA) was exploited to create stable hydrophilic surfaces in PDMS microfluidic devices.[32] A final washing step was performed with deionized water to remove all trace of contaminations in the micro-channels. Details of the surface modification have been reported in our recent publication.[28] It is noted that the oxygen permeability of a surface-modified PDMS substrate significantly differs from that of the original PDMS.[33-35] The oxygen transfer barriers at the water/PDMS interfaces can be reduced 250-fold after a 5 min plasma treatment compared with those at the original water/PDMS interface.[35] Furthermore, the layer-by-layer polyelectrolyte deposition on micro-channel wall can add additional diffusive resistance to the gas transfer from the ambient air owing to the lowered permeability of the composite layer. Water and oil were loaded in gas-tight glass syringes and delivered into the microfluidic device via a syringe pump (SPM 100 S-FLUIDPUMP, Singapore). A high-speed camera (Micro 3, Vision Research) mounted on an inverted microscope (Nikon Ti-E, Japan) was used to record the droplet coalescence images. Droplets were generated using the flow-focusing configuration shown in Figure 1. The frequencies of droplet generation were 16 ± 1 Hz. The average diameters of droplets were 72.2 ± 0.8 μm. The subsequent droplet collision and coalescence were observed at the expansion.

Figure 2 illustrates the quantification of coalescence time from videos. Videos of droplet coalescence were recorded at a frame rate of 13,000 frames per second (fps) and subsequently processed with ImageJ (V1.48, NIH, USA). One hundred coalescence events were recorded for each system to obtain the distribution of the coalescence time. At the before-contact interaction, the two droplets were still far away and approached with each other with an approximate constant velocity. When the central film thickness between the

droplet surfaces fell below a certain value (~7 μm), the relative approach velocity started decaying exponentially. When the droplets touched with each other, as seen on the video frames, the contact interaction started. Typically, the first touching occurred at a central film thickness of $\Delta h = 1$ μm which is the resolution of the camera system employed. At these large thicknesses, the before-contact interaction was not affected by intermolecular forces such as those of the van der Waals interaction and the electrical double-layer interaction. At the contact interaction, the hydrodynamic resistance in the presence of the intervening liquid film increased significantly and the film slowly drained under the influence of the capillary and intermolecular forces. The contact interaction normally ended with the film rupture, which quickly merged the droplets into one larger droplet as seen on the video frames.

The outlined qualitative analysis of the before-contact and contact interaction between two droplets has allowed us to define the onset of coalescence at time $t = T_1$ when the first touching between the droplets was detected by observing the relative motion of droplets on the videos frame by frame. This determination of coalescence onset is limited by the optical resolution of the camera system employed which is $\Delta h = 1$ μm, as shown in Figure 2. The onset usually happened between two sequential video frames, and hence the video frame rate (0.077 ms) is the temporal limit of our determination of the coalescence onset. Combining both the spatial and temporal resolutions, we can establish here that $T_1 = t\left(\Delta h \pm 1\mu\text{m}\right) \pm 0.077$ ms Likewise, by observing the first merging of the two droplets on videos frame by frame, we could also define the end of coalescence at time $T_2 = t \pm 0.077$ ms as shown in Figure 2. Knowing the start and end of the coalescence, the measured coalescence time, t_c, was calculated by $t_c = T_2 - T_1$. Since the temporal limit of 0.077 ms is significantly shorter than the coalescence time by three orders of magnitude, our determination of the first touching and merging between tow droplets from the video images is accurate and is acceptable. We will describe the details about our determination of model drainage time in the theoretical Section.

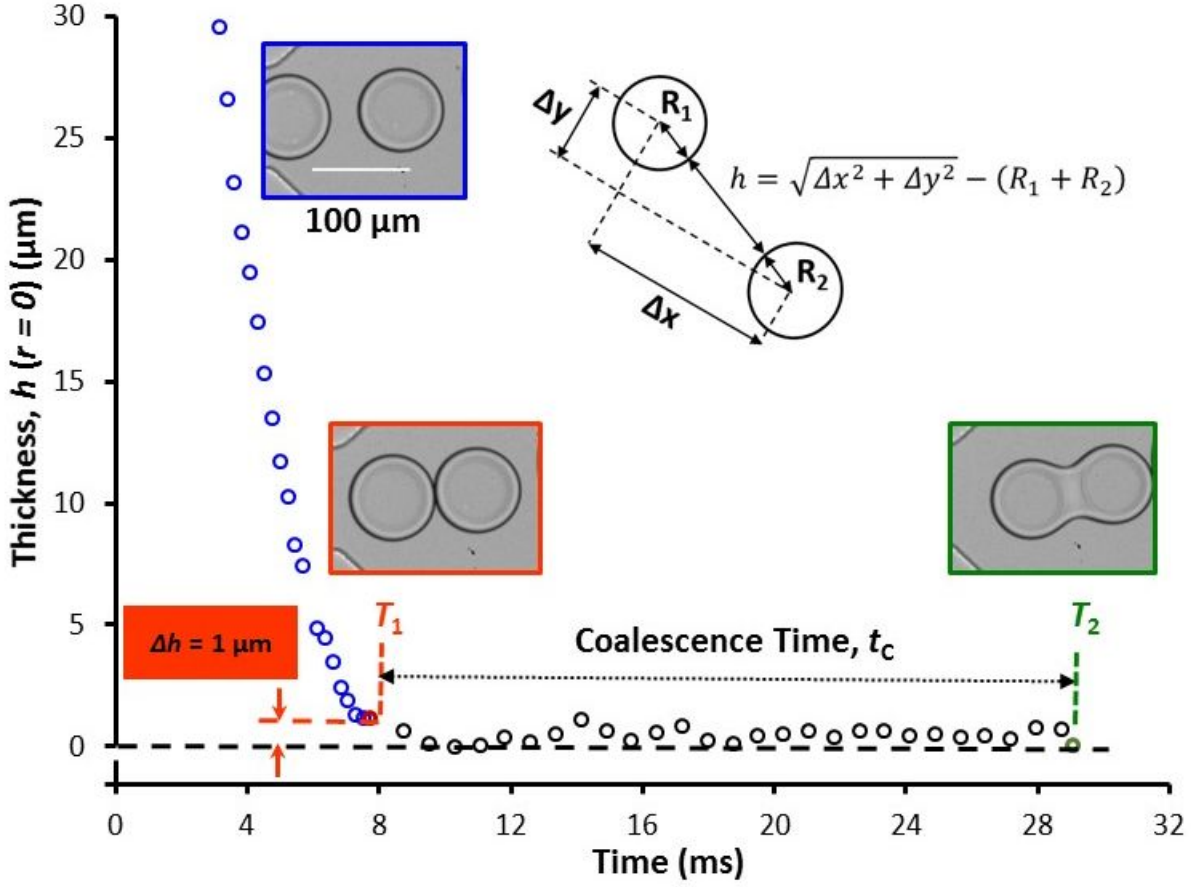

Figure 2. Consecutive stages of interaction between coalescing droplets as probed by the shortest thickness between the droplet surfaces: i) the before-contact interaction ($t<T_1$, blue circles), ii) the contact interaction with an intervening liquid film ($T_1 \leq t<T_2$, black circles), and iii) the film rupture with merging of droplets ($t = T_2$, green line). The transition between these stages was one imaging frame (0.077 ms). The coalescence time was the duration of the contact interaction, i.e., $t_c = T_2 - T_1$.

THEORY

Effect of IGEs on oil droplet interactions. The coalescence dynamics is governed by the film drainage and rupture processes. Since the film rupture is much faster than the film drainage the coalescence time is principally determined by the drainage process, which is our modelling focus. The film drainage process is determined by fluid dynamics, surface (intermolecular) forces and surface deformation. When the droplets are still far away from each other, the hydrodynamic interaction due to the motion of the fluid initially dominates the film drainage. As the droplets approach to a small thickness, the surface forces start to dominate and control the coalescence process.

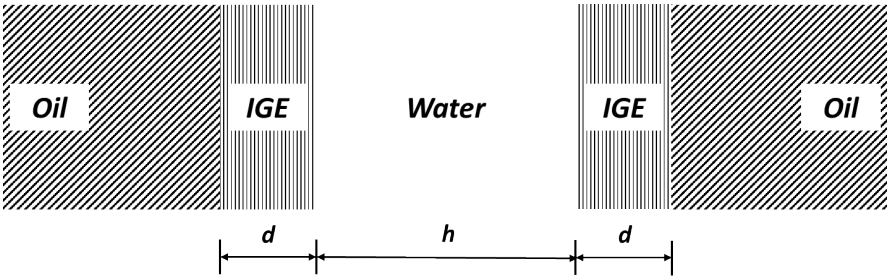

Figure 3. A model system to account for the effect of IGE on the droplet coalescence via the van der Waals interaction (not to scale). The IGEs do not retard the electromagnetic waves as strongly as water, leading to a stronger van der Waals attraction. Indeed, the van der Waals attraction between surfaces in air is stronger than in water by an order of magnitude.

We consider the effect of IGE on the drainage and coalescence by applying the van der Waals interaction [21]. The intrinsic gas layer (IGE) at water- hydrophobic interfaces has been observed by neutron reflectivity experiments[23, 36], and analyzed by molecular dynamics simulation[22]. The creeping flow condition in micro-channels minimizes hydrodynamic disturbance on the stability of IGE. Therefore, the creeping flow around droplets at the drainage stage in the micro-channels is not expected to significantly disturb the stability of the thin IGE layers. It presents the main advantage of our experiments using the microfluidic device, which is the capable of producing micro-sized droplets, moving at extremely slow speed. Therefore, we assume IGE as a uniform gas layer. Figure 3 shows the IGEs with thickness, d, confined between the water film of thickness, h, and the oil droplets. Here, we consider different length scales of the oil droplet size (100 μm), the film thickness (1 μm) and IGE (1 nm), and apply local planar geometry approximation to the oil-IGE-water-IGE-oil interaction. The van der Waals pressure was calculated using the full dielectric spectra of water and squalene available in the literature[37-38] (also given in the Supporting Information). The Derjaguin approximation is used to calculate the interaction energy between curved interfaces from their planar counterparts.[39-40] Based on these approximations, the (disjoining) pressure of the van der Waals attraction, Π_{vdW}, between two oil droplets separated by the water film with IGEs, as illustrated in Figure 3, can be calculated using:

$$\Pi_{vdW}(h) = -\frac{A}{6\pi h^3}, \qquad (1)$$

where A is the Hamaker function of the thickness due to the effect of the speed of light propagating through the water film and IGEs (known as the retardation effect). Applying the generalized Hamaker-Lifshitz theory for the multilayer system [41] gives:

$$A = -\frac{3k_B T}{2} \sum_{n=0}^{\infty}{}' \int_{x_n}^{\infty} x \ln\left[\left\{1-\Im\left(i\omega_n\right)e^{-x}\right\}\left\{1-\overline{\Im}\left(i\omega_n\right)e^{-x}\right\}\right]dx, \quad (2)$$

where x is the dummy variable, k_B is the Boltzmann constant, and T is the absolute temperature. The prime against the summation indicates that the zero-frequency (n = 0) term is divided by 2. The Matsubara (sampling, discrete equally spaced) frequencies are described by $\omega_n = 2n\pi k_B T / \mathsf{h}$ where h is the Planck constant (divided by 2π), $i\omega_n$ represents the imaginary frequencies. $x_n = 2h\omega_n\sqrt{\varepsilon_m\left(i\omega_n\right)}/c$, where c is the speed of light and $\varepsilon_m\left(i\omega_n\right)$ describes the dielectric susceptibility of a material m, which refers to the central material across which the layered structures interact (i.e. water phase for this study). $\sqrt{\Im}$ and $\sqrt{\overline{\Im}}$ describe the diamagnetic reflection coefficients and the dielectric reflection coefficients of a photon passing through the water film and IGEs from one droplet to another, respectively. We consider the formation of IGE (A) with thickness d next to the oil surface (O) acting across the water film (W) with thickness of h, and have the following expression:

$$\sqrt{\Im\left(i\omega_n\right)} = \frac{\Delta_{WA} + \Delta_{AO}\exp\left[-xds_A/\left(hq\right)\right]}{1+\Delta_{WA}\Delta_{AO}\exp\left[-xds_A/\left(hq\right)\right]}, \quad (3)$$

In Eq. (3), Δ_{WA} and Δ_{AO} are the diamagnetic reflection coefficients of a photon passing across a single interface between two materials, and are given by:

$$\Delta_{jk} = \frac{s_j - s_k}{s_j + s_k}, \quad (4)$$

where the subscripts j, k refers to the two materials, and the retardation coefficients, s_j, are defined by the following generic expression:

$$s_j = \sqrt{q^2 - 1 + \varepsilon_j\left(i\omega_n\right)/\varepsilon_m\left(i\omega_n\right)}, \quad (5)$$

where $\varepsilon_j(i\omega_n)$ describes dielectric susceptibility of a material *j*, which refers to the particular material of each layer, i.e., oil or air for this study and the dielectric susceptibility of air, $\varepsilon_A(i\omega_n)=1$. The oil and water susceptibilities are given in the Supporting Information (Figures S1 and S2). In Eq. (5), parameter *q* is defined as follows:

$$q=\frac{xc}{2\omega_n h\sqrt{\varepsilon_m(i\omega_n)}}, \tag{6}$$

$\sqrt{\Im}$ in Eq. can be calculated using Eq. (3) with symbol Δ being replaced by $\overline{\Delta}$, which are the dielectric reflection coefficients of a photon passing across a single interface between the two materials, and is given by:

$$\overline{\Delta}_{jk}=\frac{s_j\varepsilon_j(i\omega_n)-s_k\varepsilon_k(i\omega_n)}{s_j\varepsilon_j(i\omega_n)+s_k\varepsilon_k(i\omega_n)}, \tag{7}$$

The numerical calculation of Eq. (2) was performed using the Gauss-Laguerre quadrature.[39] The computational results were obtained using the values of the zeros of the Laguerre polynomial and the respective weights of the 30th order Gauss-Laguerre quadrature. The computation of the outer summation included at least 3000 terms for satisfactory convergence and accuracy.

Incorporating IGE into droplet coalescence. The effect of IGE on the droplet coalescence through the film drainage process (Figure 4) is affected by the disjoining pressure $\Pi(h)$. The van der Waals pressure is a significant component of $\Pi(h)$ as per the DLVO (Derjaguin-Landau-Verwey-Overbeek) theory. Modelling of the film drainage process, $\frac{\partial h}{\partial t}$, based on the lubrication approximation to the Stokes equation is well described in the literature,[39] and the governing differential equations and initial/boundary conditions are summarized below.

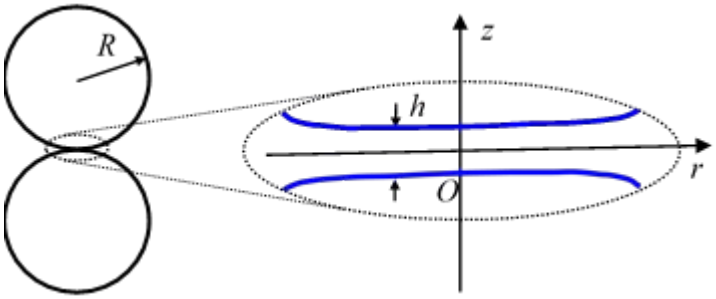

Figure 4. Definition sketch for thin film between two droplets.

The film drainage rate between two droplets is given by:

$$\frac{\partial h}{\partial t} = \frac{1}{12\mu r}\frac{\partial}{\partial r}\left\{ rh^3 \frac{\partial P}{\partial r} \right\}, \tag{8}$$

where μ is the dynamic viscosity, r is the radial coordinate, and t is the film drainage time. The immobile ('no-slip') boundary condition of Eq. (8) has been shown to be consistent with AFM measurements of bubble pair interactions on the micro scale.[42] It is noted that the inevitable trace impurities tend to arrest interfacial mobility[43] and the mobile interface is difficult to achieve for drops and bubbles in the μm size range.[44] The excess pressure, P, inside the film relative to the bulk is given by the augmented Young-Laplace equation:

$$P(h,r) = \frac{2\sigma}{R} - \frac{\sigma}{r}\frac{\partial}{\partial r}\left\{ r\frac{\partial h/\partial r}{\sqrt{1+(\partial h/\partial r)^2}} \right\} - \Pi(h), \tag{9}$$

where σ is the interfacial tension between water and oil (no IGE) or between water and air (with IGE), and R is the droplet effective radius. Eqs. (8) and (9) can be converted into the following dimensionless forms:

$$\frac{\partial y}{\partial \tau} = \frac{1}{12\rho}\frac{\partial}{\partial \rho}\left\{ \rho y^3 \frac{\partial p}{\partial \rho} \right\}, \tag{10}$$

and

$$p(\rho,y)=2-\frac{1}{2\rho}\frac{\partial}{\partial\rho}\left\{\rho\frac{\partial y}{\partial\rho}\right\}-\wp(y), \tag{11}$$

where $\rho=\frac{r}{R}Ca^{-1/4}$, $y=\frac{h}{R}Ca^{-1/2}$, $p=\frac{R}{\sigma}P$, $\tau=\frac{\sigma\sqrt{Ca}}{R\mu}t$, $\wp=\frac{R}{\sigma}\Pi$, $y_0=\frac{h_0}{R}Ca^{-1/2}$, and $\tau_0=\frac{\sigma\sqrt{Ca}}{R\mu}t_0$. Here, h_0 is the initial film thickness at the film center. The capillary number, $Ca=\mu V/\sigma$, is defined using a velocity constant, V.

At the beginning of film drainage, the two droplets are still far away from each other and their deformation is negligible. Therefore, their initial shape close to the axis can be approximated by a parabolic profile and described as follows:

$$y(\rho,\tau=0)=y_0+\rho^2 \tag{12}$$

In our numerical solution, we define the start of film drainage at $t = 0$ when the velocity of the droplet surface at the outer boundary of the water film starts to follow the initial condition: $\frac{\partial h}{\partial t}=-V\exp(-t/t_0)$ at the (initial) film thickness of 7 μm as described in the experimental Section. It is noted that the velocity constant, V, and the time constant, t_0, can be accurately determined by fitting the experimental data, i.e., h vs t. An example of the experimental data and fitting details can be found in the Supporting Information (Figure S3). In terms of dimensionless variables, the dimensionless form of the initial condition can be described as follows:

$$\frac{\partial y}{\partial\tau}=-\exp(-\tau/\tau_0), \tag{13}$$

where τ_0 is the dimensionless form of a time constant t_0. The excess pressure in liquid film equals to zero, i.e.:

$$p(\rho,y,\tau=0)=0 \tag{14}$$

The boundary conditions at the axis of symmetry and film boundary are described as follows:

$$\left(\frac{\partial y}{\partial \rho}\right)_{\rho=0}=0,\ \left(\frac{\partial p}{\partial \rho}\right)_{\rho=0}=0,\ \ p(\rho\to\infty,y)=0, \tag{15}$$

The computational domain for solving the drainage equation is now fully enclosed.

Double-layer disjoining pressure. In addition to the van der Waals pressure, the total disjoining pressure, $\Pi(h)$, in Eq. (9) also includes the double-layer disjoining pressure, $\Pi_{EDL}(h)$, as per the DLVO theory. It can be expressed as a function of water film thickness as follows:[45]

$$\Pi_{EDL}(h)=\frac{32Ck_BT}{\kappa}\times\tanh^2\left(\frac{\Phi}{4}\right)\times\left\{\frac{\kappa}{2}\operatorname{sech}^2\left(\frac{\kappa h}{2}\right)+f(\Phi)\kappa\sinh^2\left(\frac{\Phi}{4}\right)\exp\left[-f(\Phi)\kappa h\right]\right\}, \tag{16}$$

where $f(\Phi)=2\cosh\left(0.332|\Phi|-0.779\right)$, $\Phi=ze\psi_s/(k_BT)$ is the reduced surface potential for $|\Phi|\le 7$, ψ_s is the film surface potential, e is the charge of an electron, k_B is the Boltzmann constant, T is the absolute temperature, C is the number concentration of z:z salt ions, and κ is the Debye constant. At 25°C, $\kappa=3.288\sqrt{I}$ where κ is measured in nm^{-1}and the ionic strength, I, is measured in mol/L. For DI water at unadjusted nature pH = 5.8, I = 2.5×10^{-6} mol/L because of dissolved CO_2 from the ambient atmosphere. We do not expect any significant change in the charge state of the oil-droplet surface as the quantity of gas is decreased, simply because of the non-ionic nature of the dissolved gas molecules. We only consider two different charging conditions equivalent to the special cases studied here, i.e., 1) water/squalene interface with a surface (zeta) potential of -27.5 mV [46] and 2) water/IGE (air) interface with a zeta potential of -65.0 mV [47]. The first condition applies to the degassed system, i.e., IGE thickness = 0, and the second state applies to the non-degassed systems

where IGE thickness $\neq$ 0.

Numerical procedure. The partial differential equations for the film drainage as described by Eqs. (10) and (11) together with the initial and boundary equations, can be solved numerically by the method of lines with the spatial derivative being approximated using a finite difference scheme. This method yields a system of differential-algebraic equations of index 1, which can be solved by employing a standard numerical package such as ODE15s in Matlab. The boundary condition at infinity is applied at a significantly large distance (typically, at ρ = 15), beyond which the film thickness profile does not change significantly. The van der Waals pressure can be numerically calculated explicitly for different film thicknesses and IGE thicknesses, prior to solving the partial differential equation by the method of lines. The numerical data can then be interpolated to provide the van der Waals pressure needed for solving Eqs. (10) and (11). The interpolation procedure can significantly reduce the computational resources and time.

RESUTLS AND DISCUSSION

Experimental coalescence time vs dissolved oxygen concentration

Figure 5 shows the measured coalescence time distributions for oil droplets with two different amounts of dissolved oxygen (7.89 mg/L and 4.59 mg/L). The measured coalescence times were found to be in the range 15 - 23 ms for 7.89 mg/L of dissolved oxygen, and 44 - 57 ms for 4.59 mg/L of dissolved oxygen. The Gaussian fits gave the values of corresponding mean of coalescence time, $\bar{\mu}$, 18.71 and 50.24 ms, and standard deviation, $\bar{\sigma}$, 1.78 and 3.12 ms, respectively. It can be seen that mean coalescence time was increased with decreased dissolved oxygen concentration. The film rupture is very fast (much faster than the film drainage), therefore the rupture (time) does not significantly contribute to the coalescence time. The origin of coalescence time distribution comes from different factors, such as droplet size variation, asymmetrical droplet deformation during collision depending on the shear flow and collision angle.[48] A reported probability distribution of critical film thickness in a quiescent emulsion may contribute to the observed coalescence time distribution.[49-50]

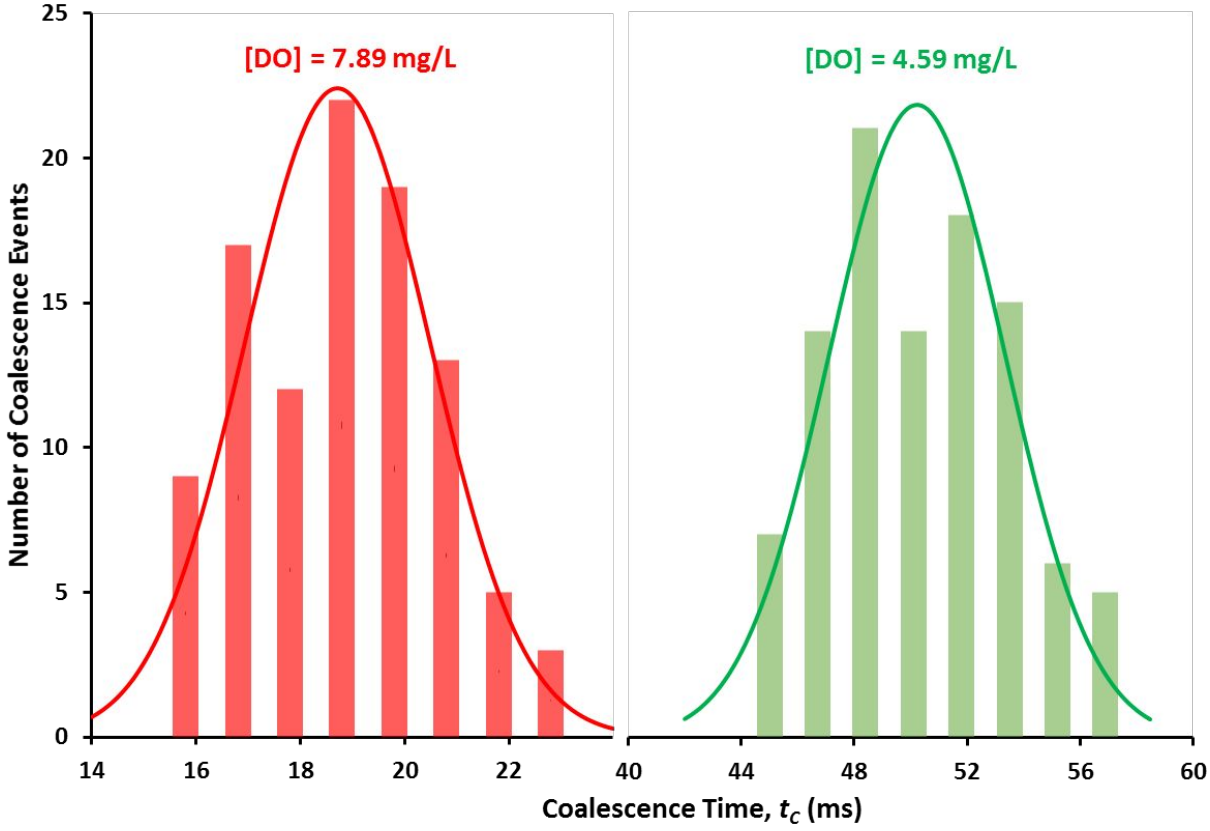

Figure 5. Experimental coalescence time distributions vs dissolved oxygen concentration [DO], displaying significant impact of dissolved gases.

Simulated film thickness vs time, radial position and presence of IGE layer

Figure 6 shows numerical model prediction of film profiles as a function of time for systems with 4.9 and 5.5 nm IGE, respectively. The fastest decrease in film thickness occurs at the film center (i.e., at $r = 0$ as shown in Figure 4). The simulation stops at $T_2 = 50$ and 20 ms, respectively. The termination of simulation is because the film thickness becomes negative (MatLab crashes as the Hamaker constant, A, does not exist when film thickness becomes negative) at the next time step, respectively, indicating the film rupture (coalescence) may occur between these two time steps. Typically, the certainty of our modelling results for dimensionless coalescence time is $\tau = 1$ (0.03 ms).

To match our experimental determination of coalescence time, we also defined the onset of coalescence from our theoretical calculation at the model film thickness of 1 μm, i.e., $T_1 = t(\Delta h)$ as shown in Figure 6 and in the experimental determination of the coalescence

onset. Our certainty analysis described at the end of this Section shows that indeed the theoretical onset of coalescence as defined at 1 μm film thickness is accurate. It is because the film drainage process is slow and the time of film drainage is significantly longer than the model time step of 0.03 ms.

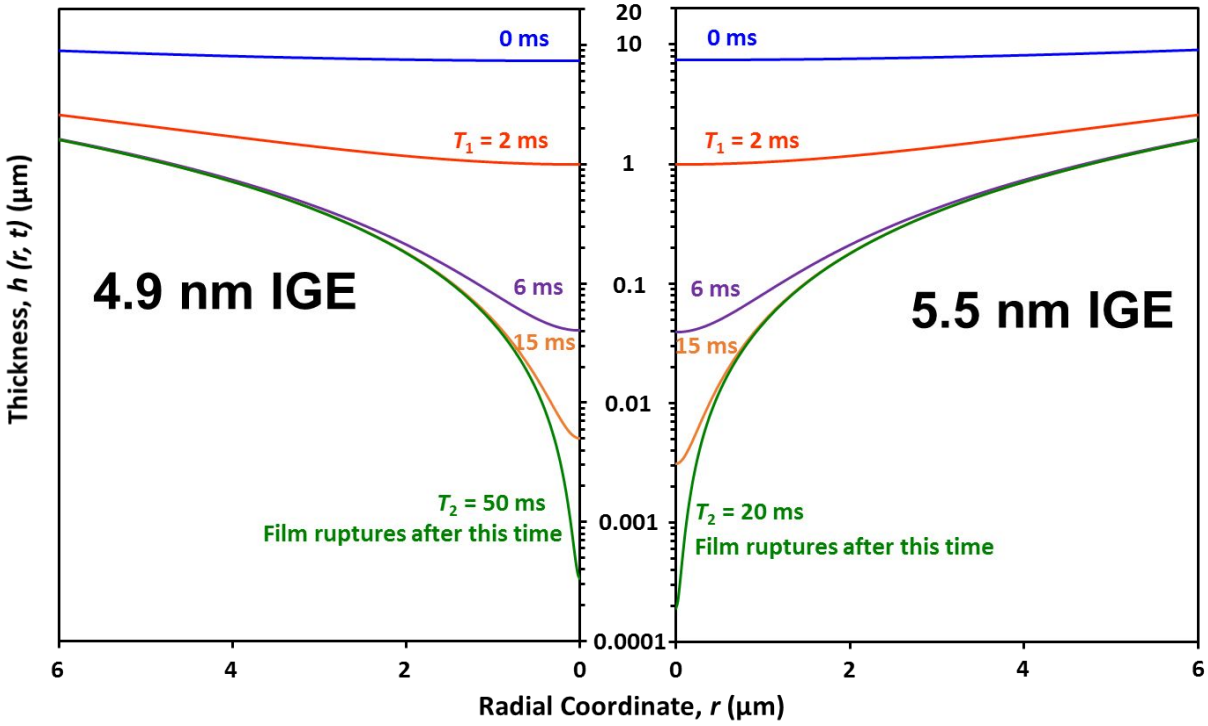

Figure 6. Computed temporal film profiles for coalescing systems with IGE = 4.9 and 5.5 nm, respectively. The coalescence time is calculated as follows: $t_c = T_2 - T_1$. The additional input parameters include $R = 22.6$ μm, $\mu = 1$ mPa s, $V = 7.25$ mm/s and $t_0 = 1.02$ ms.

It can be seen in Figure 6 that film drainage rate increases with increased IGE thickness. The model coalescence times ($t_c = T_2 - T_1$), 18 and 48 ms are close to measured values, 18.71 and 50.24 ms for 7.89 and 4.59 mg/L of dissolved oxygen, respectively. The computed coalescence time are consistent with the measured values in Figure 5, where the system with higher amount of dissolved oxygen (larger IGE thickness) has shorter coalescence time (faster film drainage dynamics).

Figure 7 shows the effect of IGE thickness on film drainage dynamics and comparison of the computed coalescence times (drainage time from 1 μm film thickness until film

rupture) and the measured values. We assume that the film ruptures at 1 nm, where the thickness decreases sharply. Again, it can be seen that the film drainage rate increases with increased IGE thickness. When the system is totally degassed (IGE thickness = 0 nm), the film reaches to an equilibrium thickness of 30 nm. This result is consistent with previous studies on the enhanced emulsion stability by removing the dissolved gases.[51] When the IGE thickness increases from 0 nm to 4 nm, the equilibrium thickness decreases from 30 nm to 7 nm due to the increased capillary and van der Waals forces (Figure S4 in the Supporting Information). The complete degassing result in full droplet stability (perhaps, with unchanged or lower value of surface charge and electrical double layer repulsion). Therefore, the effect of dissolved gases on droplet stability is not due to the surface charge. Instead, the droplet stability depends on the effect of the interfacial gas layer on the van der Waals forces, which in turn changes the disjoining pressure and the film drainage kinetics. The film rupture occurs when the IGE thickness reaches to 4.8 nm, above which the coalescence time becomes highly sensitive to the IGE thickness. For example, the coalescence time decreases sharply from 62 to 14 ms when the IGE thickness just increases from 4.8 nm to 6.0 nm. The computed coalescence times for systems with 5.5 and 4.9 nm IGE are closest to the measured values. Reported neutron reflectivity measurements revealed that the introduction of dissolved gases lead to the increase in IGE thickness [23, 36]. Our results which show that 4.9 and 5.5 nm IGEs correspond to 4.59 and 7.89 mg/L dissolved oxygen would be consistent with the reported relationship between IGE thickness and dissolved gas concentration.

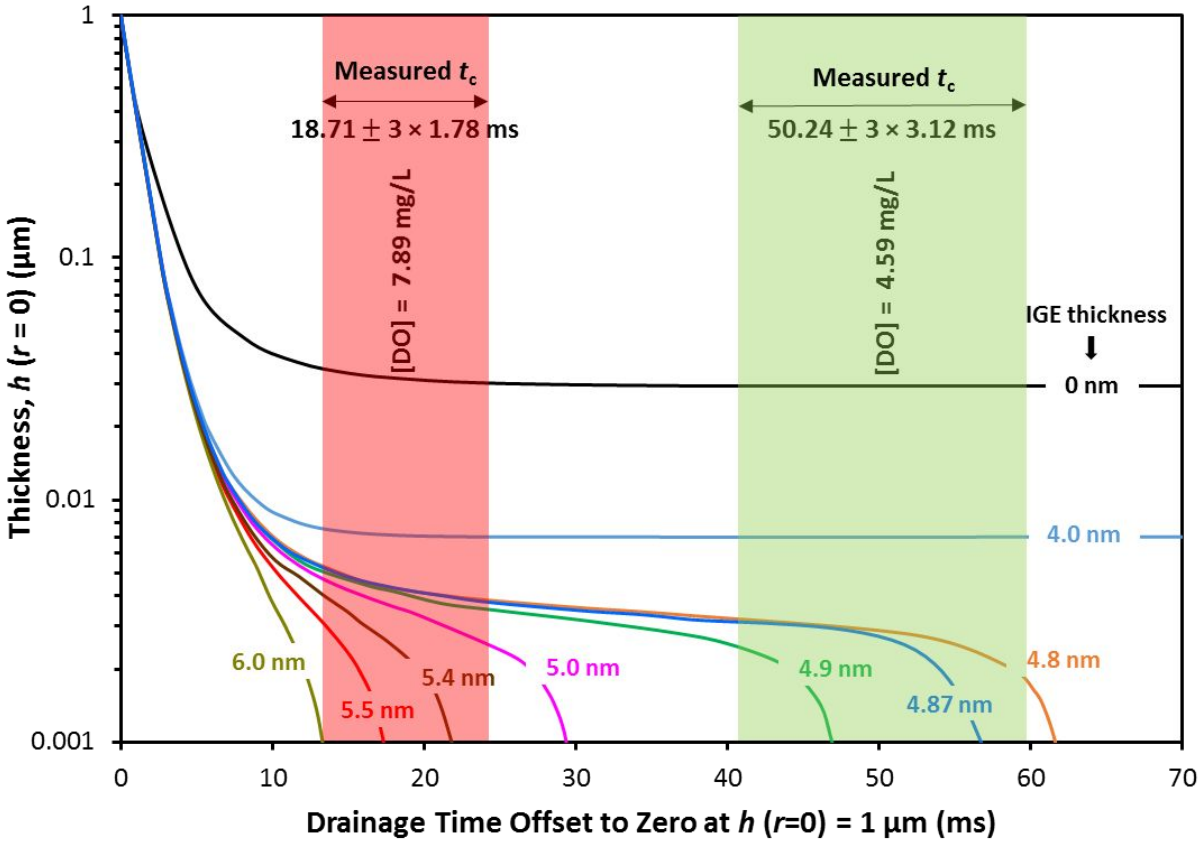

Figure 7. Effect of IGE thickness on film thickness at the center as a function of the drainage time being offset to zero at the initial thickness of 1 μm. The shaded areas show the two ranges of the measured coalescence time with the mean and $3\overline{\sigma}$ (i.e., 99.7% of certainty).

It is worth noting that due to our experimental resolution the initial film thickness at the beginning of coalescence is about 1 μm, which is used in determining the coalescence time in our modelling, $t_c = T_2 - T_1$. It is critical to examine the effect of the initial film thickness used to offset the drainage time zero in the modelling. Table 1 shows the effect of possible initial film thickness to offset zero drainage time on computed coalescence times for systems with different IGE thicknesses. The change of coalescence time relative to the value at h_i = 1 μm is within 3% and 6% when the initial film thickness changes from 1 μm to 0.7 μm and to 2.0 μm, respectively. The insignificant change in computed coalescence time justifies our choice of initial film thickness (1 μm) to offset zero drainage time in determining the coalescence time.

Table 1. Effect of possible film thickness, Δh, used to offset drainage time on the computed coalescence times for systems with different IGE thicknesses. Values in bracket indicate the change of coalescence time relative to the value at $\Delta h = 1$ μm

Δh (μm)	0.7	1.0	2.0
$t_{C\_4.80}$ (ms)[1]	61.35 (-0.51%)	61.66 (0.00%)	62.42 (+1.22%)
$t_{C\_4.87}$ (ms)	56.48 (-0.55%)	56.80 (0.00%)	57.55 (+1.32%)
$t_{C\_4.90}$ (ms)	46.67 (-0.67%)	46.99 (0.00%)	47.74 (+1.60%)
$t_{C\_5.00}$ (ms)	29.04 (-1.07%)	29.36 (0.00%)	30.11 (+2.56%)
$t_{C\_5.40}$ (ms)	21.52 (-1.43%)	21.83 (0.00%)	22.58 (+3.44%)
$t_{C\_5.50}$ (ms)	17.09 (-1.80%)	17.41 (0.00%)	18.16 (+4.31%)
$t_{C\_6.00}$ (ms)	13.04 (-2.34%)	13.35 (0.00%)	14.10 (+5.62%)

[1.] The subscripts describe the IGE thickness in nm.

CONCLUSIONS

Significant effect of interfacial gas enrichment (IGE) on the droplet coalescence was studied by microfluidics and solving film drainage equations. We observed a faster coalescence between two individual droplets in a microfluidic channel, where the oil is gassed. This observation led us to investigate the effect of IGEs on the coalescence dynamics using the DLVO approach. The IGEs do not retard the electromagnetic wave as strongly as water, leading to a stronger van der Waals attraction. The computed coalescence time show that the gassed systems have faster coalescence dynamics because of the stronger van der Waals and capillary forces. Both the measured and computed results show that the coalescence rate is proportional to the amount of dissolved gases (IGE thickness). In contrast, the coalescence can be prevented in the degassed systems. Our study provides an alternative approach to investigate the relationship between dissolved gases and "hydrophobic" interactions. Essentially, the "hydrophobic" interactions in the presence of dissolved gases are the enhanced DLVO interactions due to the formation of IGEs. In future work, in-situ degassing methods will be developed to achieve better control of dissolved gas concentrations.

ACKNOWLEDGEMENT

N.T.N., A.V.N. and G.M.E. acknowledge funding support from Australian Research Council through projects DP140101089 and DP170100277. S.H Tan gratefully acknowledges

the support of the Australian Research Council (ARC) Discovery Early Career Researcher Award (DECRA) (DE170100600).

SUPPORTING INFORMATION

Documents: Dielectric spectra of water and squalene for calculating the Hamaker function (Figures S1 and S2); an example of fitting details (Figure S3); and variation of the Hamaker function vs thickness of film and IGE (Figure S4).

Videos (avi): The combined video compares the coalescence between two 72.5-μm-diameter oil droplets in a gassed system (top), and coalescence between two oil droplets (73.0 μm diameter) in partially degassed system (bottom). The video was recorded at 13,000 fps and played at 30 fps.

NOTES

The authors declare no competing financial interests.

REFERENCES

1. Israelachvili, J. N.; Pashley, R. M., Measurement of the hydrophobic interaction between two hydrophobic surfaces in aqueous electrolyte solutions. *Journal of Colloid and Interface Science* **1984,** *98* (2), 500-514.
2. Claesson, P. M.; Blom, C. E.; Herder, P. C.; Ninham, B. W., Interactions between water—stable hydrophobic Langmuir—Blodgett monolayers on mica. *Journal of Colloid and Interface Science* **1986,** *114* (1), 234-242.
3. Eriksson, J. C.; Ljunggren, S.; Claesson, P. M., A phenomenological theory of long-range hydrophobic attraction forces based on a square-gradient variational approach. *Journal of the Chemical Society, Faraday Transactions 2: Molecular and Chemical Physics* **1989,** *85* (3), 163-176.
4. Meyer, E. E.; Rosenberg, K. J.; Israelachvili, J., Recent progress in understanding hydrophobic interactions. *Proceedings of the National Academy of Sciences* **2006,** *103* (43), 15739-15746.
5. Parker, J. L.; Claesson, P. M., Forces between Hydrophobic Silanated Glass Surfaces. *Langmuir* **1994,** *10* (3), 635-639.
6. Attard, P., Bridging Bubbles between Hydrophobic Surfaces. *Langmuir* **1996,** *12* (6), 1693-5.
7. Hampton, M. A.; Nguyen, A. V., Nanobubbles and the nanobubble bridging capillary force. *Advances in Colloid and Interface Science* **2010,** *154* (1–2), 30-55.

8. Rabinovich, Y. I.; Derjaguin, B. V.; Churaev, N. V., Direct measurements of long-range surface forces in gas and liquid media. *Advances in Colloid and Interface Science* **1982,** *16* (1), 63-78.
9. Yaminsky, V. V.; Yushchenko, V. S.; Amelina, E. A.; Shchukin, E. D., Cavity formation due to a contact between particles in a nonwetting liquid. *Journal of Colloid and Interface Science* **1983,** *96* (2), 301-306.
10. Christenson, H. K.; Claesson, P. M., Cavitation and the interaction between macroscopic hydrophobic surfaces. *Science* **1988,** *239* (4838), 390-392.
11. Claesson, P. M.; Christenson, H. K., Very long range attractive forces between uncharged hydrocarbon and fluorocarbon surfaces in water. *The Journal of Physical Chemistry* **1988,** *92* (6), 1650-1655.
12. Bérard, D. R.; Attard, P.; Patey, G. N., Cavitation of a Lennard-Jones fluid between hard walls, and the possible relevance to the attraction measured between hydrophobic surfaces. *The Journal of Chemical Physics* **1993,** *98* (9), 7236-7244.
13. Craig, V. S. J.; Ninham, B. W.; Pashley, R. M., The effect of electrolytes on bubble coalescence in water. *The Journal of Physical Chemistry* **1993,** *97* (39), 10192-10197.
14. Yaminsky, V. V.; Ninham, B. W., Hydrophobic force: lateral enhancement of subcritical fluctuations. *Langmuir* **1993,** *9* (12), 3618-24.
15. Wood, J.; Sharma, R., How Long Is the Long-Range Hydrophobic Attraction? *Langmuir* **1995,** *11* (12), 4797-4802.
16. Craig, V. S. J.; Ninham, B. W.; Pashley, R. M., Direct Measurement of Hydrophobic Forces: A Study of Dissolved Gas, Approach Rate, and Neutron Irradiation. *Langmuir* **1999,** *15* (4), 1562-1569.
17. Stevens, H.; Considine, R. F.; Drummond, C. J.; Hayes, R. A.; Attard, P., Effects of Degassing on the Long-Range Attractive Force between Hydrophobic Surfaces in Water. *Langmuir* **2005,** *21* (14), 6399-6405.
18. Ruckenstein, E.; Churaev, N., A possible hydrodynamic origin of the forces of hydrophobic attraction. *Journal of Colloid and Interface Science* **1991,** *147* (2), 535-538.
19. Attard, P., Long-range attraction between hydrophobic surfaces. *The Journal of Physical Chemistry* **1989,** *93* (17), 6441-6444.
20. Podgornik, R., Electrostatic correlation forces between surfaces with surface specific ionic interactions. *The Journal of Chemical Physics* **1989,** *91* (9), 5840-5849.
21. Azadi, M.; Nguyen, A. V.; Yakubov, G. E., Attractive Forces between Hydrophobic Solid Surfaces Measured by AFM on the First Approach in Salt Solutions and in the Presence of Dissolved Gases. *Langmuir* **2015,** *31* (6), 1941-1949.
22. Peng, H.; Birkett, G. R.; Nguyen, A. V., Origin of Interfacial Nanoscopic Gaseous Domains and Formation of Dense Gas Layer at Hydrophobic Solid–Water Interface. *Langmuir* **2013,** *29* (49), 15266-15274.
23. Doshi, D. A.; Watkins, E. B.; Israelachvili, J. N.; Majewski, J., Reduced water density at hydrophobic surfaces: Effect of dissolved gases. *Proceedings of the National Academy of Sciences of the United States of America* **2005,** *102* (27), 9458-9462.
24. Bresme, F.; Chacón, E.; Tarazona, P.; Tay, K., Intrinsic Structure of Hydrophobic Surfaces: The Oil-Water Interface. *Physical Review Letters* **2008,** *101* (5), 056102.

25. Firouzi, M.; Nguyen, A. V., Effects of monovalent anions and cations on drainage and lifetime of foam films at different interface approach speeds. *Advanced Powder Technology* **2014,** *25* (4), 1212-1219.
26. Karakashev, S. I.; Nguyen, A. V., Do Liquid Films Rupture due to the So-Called Hydrophobic Force or Migration of Dissolved Gases? *Langmuir* **2009,** *25* (6), 3363-3368.
27. Ata, S.; Pugh, R. J.; Jameson, G. J., The influence of interfacial ageing and temperature on the coalescence of oil droplets in water. *Colloids and Surfaces A: Physicochemical and Engineering Aspects* **2011,** *374* (1), 96-101.
28. Wang, J.; Tan, S. H.; Nguyen, A. V.; Evans, G. M.; Nguyen, N.-T., A Microfluidic Method for Investigating Ion-Specific Bubble Coalescence in Salt Solutions. *Langmuir* **2016,** *32* (44), 11520-11524.
29. Hildebrandt, E.; Dessy, A.; Sommerling, J.-H.; Guthausen, G.; Nirschl, H.; Leneweit, G., Interactions between Phospholipids and Organic Phases: Insights into Lipoproteins and Nanoemulsions. *Langmuir* **2016,** *32* (23), 5821-5829.
30. Naziri, E.; Consonni, R.; Tsimidou, M. Z., Squalene oxidation products: Monitoring the formation, characterisation and pro-oxidant activity. *European Journal of Lipid Science and Technology* **2014,** *116* (10), 1400-1411.
31. Nguyen, N.-T.; Wereley, S. T., *Fundamentals and Applications of Microfluidics*. Artech House: Boston London, 2002.
32. Bauer, W.-A. C.; Fischlechner, M.; Abell, C.; Huck, W. T. S., Hydrophilic PDMS microchannels for high-throughput formation of oil-in-water microdroplets and water-in-oil-in-water double emulsions. *Lab on a Chip* **2010,** *10* (14), 1814-1819.
33. Halldorsson, S.; Lucumi, E.; Gómez-Sjöberg, R.; Fleming, R. M. T., Advantages and challenges of microfluidic cell culture in polydimethylsiloxane devices. *Biosensors and Bioelectronics* **2015,** *63*, 218-231.
34. Mehta, G.; Mehta, K.; Sud, D.; Song, J. W.; Bersano-Begey, T.; Futai, N.; Heo, Y. S.; Mycek, M.-A.; Linderman, J. J.; Takayama, S., Quantitative measurement and control of oxygen levels in microfluidic poly(dimethylsiloxane) bioreactors during cell culture. *Biomedical Microdevices* **2007,** *9* (2), 123-134.
35. Hitoshi, S.; Takeshi, S.; Ching-Chou, W.; Tomoyuki, Y.; Masaki, Y.; Hiroyuki, A.; Tomokazu, M.; Hiroshi, Y., Oxygen Permeability of Surface-modified Poly(dimethylsiloxane) Characterized by Scanning Electrochemical Microscopy. *Chemistry Letters* **2006,** *35* (2), 234-235.
36. Steitz, R.; Gutberlet, T.; Hauss, T.; Klösgen, B.; Krastev, R.; Schemmel, S.; Simonsen, A. C.; Findenegg, G. H., Nanobubbles and Their Precursor Layer at the Interface of Water Against a Hydrophobic Substrate. *Langmuir* **2003,** *19* (6), 2409-2418.
37. Hayashi, H.; Hiraoka, N., Accurate Measurements of Dielectric and Optical Functions of Liquid Water and Liquid Benzene in the VUV Region (1–100 eV) Using Small-Angle Inelastic X-ray Scattering. *The Journal of Physical Chemistry B* **2015,** *119* (17), 5609-5623.
38. Painter, L. R.; Attrey, J. S.; Jr., H. H. H.; Birkhoff, R. D., Vacuum ultraviolet optical properties of squalane and squalene. *Journal of Applied Physics* **1984,** *55* (3), 756-759.

39. Nguyen, A. V.; Schulze, H. J., *Colloidal science of flotation*. Marcel Dekker: New York, 2004; Vol. 118.
40. Israelachvili, J. N., *Intermolecular and Surface Forces*. 3rd ed.; Elsevier: Sydney, 2011.
41. Parsegian, V. A.; Ninham, B. W., Van der Waals forces in many-layered structures: Generalizations of the lifshitz result for two semi-infinite media. *Journal of Theoretical Biology* **1973,** *38* (1), 101-109.
42. Tabor, R. F.; Grieser, F.; Dagastine, R. R.; Chan, D. Y. C., Measurement and analysis of forces in bubble and droplet systems using AFM. *Journal of Colloid and Interface Science* **2012,** *371* (1), 1-14.
43. Chan, D. Y. C.; Klaseboer, E.; Manica, R., Dynamic deformations and forces in soft matter. *Soft Matter* **2009,** *5* (15), 2858-2861.
44. Kelsall, G. H.; Tang, S.; Smith, A. L.; Yurdakul, S., Measurement of rise and electrophoretic velocities of gas bubbles. *Journal of the Chemical Society, Faraday Transactions* **1996,** *92* (20), 3879-3885.
45. Nguyen, A. V.; Evans, G. M.; Jameson, G. J., Simple Approximate Expressions for Electrical Double-Layer Interaction at Constant Moderate Potentials. *Journal of Colloid and Interface Science* **2000,** *230* (1), 205-209.
46. Fox, C. B.; Baldwin, S. L.; Duthie, M. S.; Reed, S. G.; Vedvick, T. S., Immunomodulatory and physical effects of oil composition in vaccine adjuvant emulsions. *Vaccine* **2011,** *29* (51), 9563-9572.
47. Nguyen, P. T.; Nguyen, A. V., Drainage, Rupture, and Lifetime of Deionized Water Films: Effect of Dissolved Gases? *Langmuir* **2010,** *26* (5), 3356-3363.
48. Krebs, T.; Schroen, C. P. G. H.; Boom, R. M., A microfluidic study of oil-water separation kinetics. *WIT Trans. Eng. Sci.* **2012,** *74* (Advances in Fluid Mechanics IX), 427-438.
49. Walstra, P., *Physical Chemistry of Foods*. Chapman and Hall/CRC: Baton Rouge, UNITED STATES, 2002.
50. Ivanov, I. B.; Danov, K. D.; Kralchevsky, P. A., Flocculation and coalescence of micron-size emulsion droplets. *Colloids and Surfaces A: Physicochemical and Engineering Aspects* **1999,** *152* (1), 161-182.
51. Maeda, N.; Rosenberg, K. J.; Israelachvili, J. N.; Pashley, R. M., Further Studies on the Effect of Degassing on the Dispersion and Stability of Surfactant-Free Emulsions. *Langmuir* **2004,** *20* (8), 3129-3137.

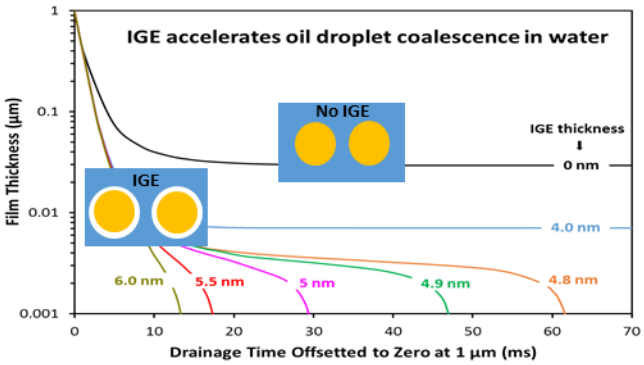
IGE accelerates oil droplet coalescence in water
No IGE
IGE
IGE thickness
0 nm
4.0 nm
6.0 nm
5.5 nm
5 nm
4.9 nm
4.8 nm
Film Thickness (µm)
Drainage Time Offsetted to Zero at 1 µm (ms)
1
0.1
0.01
0.001
0
10
20
30
40
50
60
70